Energy & Environmental Science

RSC Publishing

PAPER

View Article Online
View Journal | View Issue

Cite this: *Energy Environ. Sci.*, 2013, **6**, 2745

Electrochemical water splitting by layered and 3D cross-linked manganese oxides: correlating structural motifs and catalytic activity†

Arno Bergmann,*[a] Ivelina Zaharieva,*[b] Holger Dau[b] and Peter Strasser[a]

Manganese based precious metal-free electrocatalysts for the oxygen evolution reaction (OER) are promising materials for energy storage systems based on dark or photo-coupled water electrolysis, because they are active, inexpensive and of low toxicity. In this work, atomic scale structure–activity relationships of two different nano-structured manganese oxides, MnO_x, are established using a combination of X-ray absorption, diffraction and electrochemistry. Prepared by chemical symproportionation (s-MnO_x) and impregnation (i-MnO_x), the s-MnO_x catalyst consisted of a layered structure similar to δ-MnO_2 while the i-MnO_x catalyst displayed a mixture of tunnelled, 3D cross-linked β- and defective γ-MnO_2 structures. During electrocatalytic oxygen evolution the structural motifs of both MnO_x remain largely unchanged, but the oxidation state of Mn increases from 3.5 to 3.9–4. Kinetic parameters of the electrocatalytic oxygen evolution reaction were extracted using Tafel slope analysis and pH titration experiment, and the role of the protons abstracted was analyzed. The study reveals fundamental differences of general importance in the catalytic activity between layered and cross-linked structures. The exclusive presence of di-μ-oxo-bridged Mn ions in the layered structure is coupled to a pronounced redox and charge capacity behaviour. This ensured efficient use of surface and bulk active sites, and resulted in a relatively large Tafel slope. Consequently, the intrinsic OER activity is especially high in s-MnO_x. In contrast, 3D cross-linked structures with both mono- and di-μ-oxo-bridged Mn ions resulted in lower intrinsic activity but smaller Tafel slope, and thus favourable activity at technological water-splitting rates. The insights from this comparative study will provide guidance in the structural design and optimization of other non precious metal oxide OER catalysts.

Received 8th April 2013
Accepted 9th July 2013

DOI: 10.1039/c3ee41194j

www.rsc.org/ees

Broader context

The intermittency of the electrical output power of renewable solar and wind energy devices makes efficient, cost-effective, grid-scale energy storage mandatory. Electrical power storage using molecular bonds (synthesis of fuel molecules) offers a number of advantages over storage in solid state material lattices. As electrolytic synthesis of chemical fuels is a reductive chemical process, a corresponding electrooxidation process at the grid-scale level is essential. Electrochemical water oxidation to molecular oxygen is perhaps the only feasible oxidation process that can provide electrons and protons at the required grid-scale. However, inexpensive, efficient and stable water oxidation catalysts are rare, if non-existent. This is why the development of non-precious water oxidation catalysts has become a scientific priority. Manganese oxides attract special attention as water splitters, as they form the basis for Nature's oxygen evolving complex in the Photosystem II complex. Detailed insight into structure–activity relationships of inorganic Mn containing water splitting materials is still scarce. This article addresses this unmet need.

Introduction

The development of active, stable and inexpensive electrocatalysts for water splitting is a key step in the commercialization of a so-called hydrogen economy which is based on the use of molecular hydrogen for energy storage instead of fossil carbohydrates.[1] The attractive concept of direct chemical storage of solar energy may be denoted as artificial photosynthesis and is predicted to become a frontier technology in future energy sustainability.[2] To realize chemical energy storage devices for individual use or applications in developing countries, the (electro)catalysts need to be based on low toxicity and

[a]*Department of Chemistry, Chemical and Materials Engineering Division, The Electrochemical Energy, Catalysis and Materials Science Laboratory, Technische Universität Berlin, Straße des 17. Juni 124, 10623 Berlin, Germany. E-mail: bergmann@chem.tu-berlin.de; pstrasser@tu-berlin.de; Fax: +49 30-314 22261; Tel: +49 30-314 29542*

[b]*Fachbereich Physik, Freie Universität Berlin, Arnimallee 14, 14195 Berlin, Germany. E-mail: ivelina.zaharieva@fu-berlin.de; holger.dau@fu-berlin.de; Fax: +49 30 838 56299; Tel: +49 30 838 3581*

† Electronic supplementary information (ESI) available: Details on the syntheses of the supported manganese oxides as well as further experimental results on the characterization of the support, the pH dependence of MnO_x and additional XAS data and simulations. See DOI: 10.1039/c3ee41194j

earth-abundant elements such as Mn and Fe; and they have to be active under benign reaction conditions. However, the most active and stable electrocatalysts are based on precious metals like ruthenium and iridium in dimensionally stable anodes working in harsh, acidic environments which limits their application to industrial processes.[3–8]

Precious-metal free electrocatalysts have received strong attention since Nocera and co-workers reported efficient water oxidation by Co oxide (CoCat) prepared *via* anodic electrodeposition from a cobalt nitrate/phosphate buffer solution.[9] This CoCat shows promising water oxidation activity in phosphate buffer at pH 7 and a self-healing mechanism in the Co^{2+}-containing electrolyte was proposed. Several researchers studied the CoCat with respect to the synthetic route, the catalyst structure, and the mechanism of electrochemical oxygen evolution.[10–15] The CoCat can be described as a disordered molecular-like structure consisting of edge-sharing Co octahedra (or di-μ-oxo/hydroxo-bridged Co ions) which can form extended planes of cobaltates. For the CoCat the reported atomic structure of low ordered Co oxide layers appears to be largely independent of the synthesis protocol used.[12,14,15] Analogously, nickel oxide films synthesized by anodic electrodeposition from borate or phosphate buffer showed water oxidation activity and a similar structure containing mainly di-μ-oxo/hydroxo-bridged metal ions.[16,17]

For the CoCat in a neutral electrolyte, a chemical proton transfer step preceded by an electron transfer step in a quasi-equilibrium was suggested to determine the rate of oxygen evolution which agrees well with the former findings for Co-based electrocatalysts.[11,13,18]

In comparison to Co, the high abundance and low toxicity of manganese render Mn oxides as advantageous materials and make Mn-based catalysts highly favourable.[19] Biologically active Mn-containing water splitting complexes offer a possibly coincidental, yet elegant analogy. In earlier studies several Mn oxides varying in structure and oxidation state have been reported to be active for water oxidation, but the catalytic rates often were low and the catalyst remained without real practical applications.[20–28] Structure–activity relationships of water-oxidizing Mn oxides have been discussed but are clearly insufficiently understood.[21,22,29]

Like other binary transition metal oxides, manganese dioxides exhibit an exceptional variety of polymorphs relating, *inter alia*, to the small ionic radius for Mn^{4+}. The schematic presentation of Fig. 1 shows MnO_2 in layered structures with mainly edge-sharing Mn octahedra such as δ-MnO_2 (Fig. 1c) or in tunneled structures (Fig. 1a and b) with a combination of corner- and edge-sharing Mn octahedra such as β- and γ-MnO_2 with (1×1) and (2×1) tunnels respectively.[30–32]

A common structural imperfection in tunneled MnO_2 materials is the de Wolff defect – an intergrowth of β-MnO_2 chains in γ-MnO_2 and *vice versa*.[33,34] Furthermore, MnO_2 can exhibit Mn vacancies which lead to the replacement of Mn^{4+} ions by Mn^{3+} and this results in a mean oxidation state of Mn lower than 4.[35–37] The presence of Mn^{3+} ions in the lattice can additionally cause microtwinning – a growth defect of the γ-MnO_2 lattice.[30]

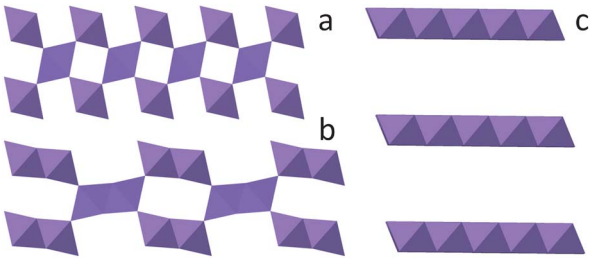

Fig. 1 Structures of selected MnO_2 modifications: β-MnO_2 (a), γ-MnO_2 (b), and δ-MnO_2 (c). The MnO_6 coordination octahedra are schematically shown. The structures are extended in the direction perpendicular to the paper plane by chains of edge-sharing octahedra (in a, b, and c). This results in (1×1) tunnels of coordination octahedra (a), in (2×1) tunnels (b), and in a layered manganese oxide (c). In the layered oxides, the interlayer space is filled with water molecules and ions.

Synthetic δ-MnO_2 consists of MnO_6 layers where the interlayer space is filled with Na^+ or K^+ ions surrounded with water molecules. In the case of an inhomogeneous distribution of the water molecules and the foreign cations, the MnO_6 layers show a "turbostratic" arrangement and thus, they are stacked without ordering.[31]

Manganese oxides have long played a crucial role in battery applications and were structurally well characterized in electrochemical battery environments.[38] For catalytically active Mn oxides both layered and tunnelled structures have been reported.[14,15,17,20,21,36] In nature, water oxidation in PSII proceeds at a metal–oxido manganese–calcium complex.[39] Recently, a synthetic Mn–Ca water oxidation catalyst has been prepared *via* a chemical synthesis route.[40] EXAFS studies revealed that in this amorphous material Mn ions are mainly interconnected *via* di-$\mu_{2/3}$-oxo-bridges and similar to δ-MnO_2 forming layers, whereas the Ca ions are positioned in the interlayer space forming Mn_3CaO_4 cubanes or compensating the charge deficiency on top of Mn-vacancies. The resulting structural motifs show striking similarities to the natural Mn–Ca complex in PSII.[22] In a subsequent study, it has been shown that other redox-inert cations can be incorporated into the layered MnO_x structure, but the obtained catalytic activity is highest when Ca ions are present.[29]

Recently, an electrolytically prepared Mn oxide (MnCat) has been presented which does not contain Ca^{2+} ions but which shows electrocatalytic activity towards oxygen evolution in neutral electrolyte. In the structure of this MnCat, together with the extensive di-μ-oxo-bridging, a significant fraction of mono-μ-oxo-bridged Mn ions was found whereas another MnO_x, electrodeposited from the same media but using different electrochemical protocols, showed almost exclusively di-μ-oxo-bridged Mn ions and had no catalytic activity.[21] It was suggested that Mn ions in lower oxidation states can play the structural (and perhaps also the functional) role of Ca in the catalytically active layered Mn oxides.

Spiccia and co-workers incorporated a synthetic tetranuclear Mn complex into a Nafion® matrix where it decomposes and forms a layered $Mn^{3+/4+}$ oxide.[41,42] Dissociation upon illumination results in disordered Mn^{2+} ions, which could be electrochemically re-oxidized to the layered, water-oxidizing $Mn^{3+/4+}$

oxide. These findings suggest that cycling through various Mn oxidation states may be crucial in water-oxidation by amorphous Mn oxides.

As opposed to the CoCat, the mechanism of water oxidation catalysed by Mn-based catalysts has been much less investigated. In the 80s, the mechanism of electrocatalytic oxygen evolution with Mn oxides in highly acidic and alkaline electrolytes was investigated using Tafel slope analysis and pH titration, and a one electron transfer step was argued to be rate-determining.[18,26,28] Recently, a mechanistic study of oxygen evolution at δ-MnO_2 in neutral electrolyte suggested that the disproportionation of Mn^{3+} to soluble Mn^{2+}may be a limiting factor for the oxygen evolution activity at neutral pH.[43] Increasing the pH above 9 was suggested to stabilize Mn^{3+} ions and to lead to a non-Nernstian potential dependence on pH during transition from neutral to alkaline reaction conditions and furthermore, to a higher oxygen evolution activity.[43]

Recently, two nano-structured manganese oxides supported on multi-walled carbon nanotubes have been developed *via* two novel synthetic routes – symproportionation–deposition reaction and incipient wetness impregnation. These materials showed promising activity and stability for electrochemical water splitting in neutral electrolyte; the initial studies indicated that the two oxides may differ in their atomic structure.[24]

In this work, we studied the structure of these two catalytically active Mn oxides after deposition and after electrochemical oxygen evolution. Our goal was to investigate the structural transformations which the two catalysts undergo during oxygen evolution reaction. The structure of as-synthesized Mn oxides and those used for electrocatalytic water oxidation were studied on different length-scales using X-ray powder diffraction (XRD), X-ray absorption near-edge structure (XANES), and extended X-ray absorption fine structure (EXAFS) spectroscopy. Furthermore, we investigated the electrocatalytic behaviour of these manganese oxides by cyclic voltammetry, Tafel slope analysis and pH titration experiments. The combination of structural information at the atomic level and comprehensive electrokinetic analysis facilitates conclusions on crucial structure–activity relationships in the synthetic Mn-oxide water-oxidation catalysts.

Experimental

Syntheses

Carbon-supported manganese oxide was synthesized *via* two different preparation methods – symproportionation deposition–precipitation (s-MnO_x) and incipient wetness impregnation (i-MnO_x).[24] The Mn concentration was determined using inductively coupled plasma-optical emission spectroscopy (ICP-OES) to be 1.69 mmol g^{-1} and 1.75 mmol g^{-1} (9.30 wt% and 9.61 wt%) for s- and i-MnO_x, respectively. Further details are given in the ESI.†

X-ray diffraction

X-ray powder diffraction was conducted on the as-prepared powders with Cu K_α radiation in reflection mode using a Bruker D8 Advance equipped with 2.3° soller slits and a position-sensitive detector (PSD).[44] Powder diffraction patterns were collected between 10° and 75° using a step size of 0.02° and a counting time of 7 s. Divergence and antiscattering slit were adjusted for a constant illuminated area.

Electrochemical characterization

The catalytically active MnO_x powders were deposited as thin films on glassy carbon (GC) rotating disk electrodes (Pine Instruments, ∅ 5 mm). Prior to the deposition GC electrodes were polished and cleaned stepwise in an ultrasonic bath using ultrapure water and acetone. 5 mg of catalyst powder was suspended in a mixture of 1.99 ml of ultrapure water, 500 μl of 2-propanol and 10 μl of Nafion® solution (5 wt% of stock solution, Sigma-Aldrich) followed by homogenization using a horn sonicator. Finally, this catalyst ink (10 μl of the catalyst suspension) was dispersed on the electrode and dried in air at 60 °C for 10 min. Thus, a Mn loading of the GC electrodes of 172.8 nmol cm^{-2} and 178.5 nmol cm^{-2} was achieved for s- and i-MnO_x, respectively.

Electrochemical measurements were conducted with a three-electrode rotating disk electrode (RDE) setup in a custom-made glass cell using a PINE® rotator and a Biologic SP-200 potentiostat. A platinum gauze acted as a counter electrode and a commercial reversible hydrogen electrode (RHE, Gaskatel) or Ag/AgCl (3 M KCl, World Precision Instruments) connected *via* a Haber–Luggin capillary was used as a reference electrode.[45,46]

Electrochemical experiments were conducted in 0.1 M phosphate buffer (KPi) at pH 7 prepared by mixing 0.1 M K_2HPO_4 (>98%, Sigma-Aldrich) and 0.1 M KH_2PO_4 (99%, Merck) aqueous solutions until the desired pH was obtained. Prior to electrochemical measurements N_2 was bubbled through the electrolyte for at least 15 min and was switched to blanketing flow during measurements. The working electrode was rotated at 1600 rpm during experiments to ensure a hydrodynamic equilibrium. Unless differently stated, all electrode potentials had been corrected for ohmic losses using electrochemical impedance spectroscopy and are referred to as RHE.

For Tafel slope analysis, current density was recorded stepwise between 1.5 and 1.9 V *vs.* RHE in a quasi-stationary mode. The electrode potential was increased and decreased in two separate experiments with steps of 20 mV hold for 5 min and both curves were averaged. To determine the ohmic resistance, impedance spectra were recorded at every potential/current step between 10 kHz and 1 Hz with a modulation amplitude of 10 mV.

To investigate the effect of pH of the electrolyte at constant current and electrode potential, different aliquots of 40 wt% KOH were added every 3 min to 0.1 M phosphate buffer and the pH was continuously measured. The initial pH of the phosphate buffer was ~4.7.

X-ray spectroscopy

XANES/EXAFS experiments were carried out at the BESSY synchrotron radiation source operated by the Helmholtz-Zentrum Berlin (HZB). The measurements at the manganese K-edge

were conducted at the KMC-1 bending-magnet beamline at 20 K in a cryostat (Oxford-Danfysik) with a liquid-helium flow system. Further details are given in ref. 21.

Samples for XAS experiments were prepared on glassy carbon cylinders, in analogy to the electrochemical RDE experiments. Electrochemical treatment in the OER range was conducted at 1.763 V *vs.* RHE for 3 min. After removal from the electrolyte under potential control, the electrode was dried immediately under air and nitrogen and immersed in liquid nitrogen where it was until XAS measurements.

Results and discussion

Structural investigations

Long-range order and morphology. Fig. 2 shows the powder X-ray diffraction pattern of s-MnO_x and i-MnO_x recorded between 10 and 75° using Cu K_α radiation. The graphite structure of the $MWNT_{ox}$ causes three strong diffraction peaks at ~25°, ~43° and ~53° (Fig. S1†).

For s-MnO_x, two asymmetric reflections at ~37° and ~66° are caused by the defective crystal structure of a δ-MnO_2 phase (space group: $C\bar{1}$). These two reflections are in good agreement with the reflections arising from regular distances within the layers consisting of edge-sharing Mn octahedra. The reflections can be assigned to the (200)/(110) and (310)/(020) doublets at ~37° and ~66°, respectively. The absence of reflections ($hkl \neq 0$), especially the strong (00l), reveals the absence of long-range order of the layer stacking. This can be induced by MnO_6 monolayers or variations in the interlayer distance due to "turbostratic" disorder.[31]

Reflection shape analysis revealed significant size-induced broadening. The integral breadth analysis of the MnO_x reflections led to a coherence length of the layers of ~6 nm. Thus, s-MnO_x is structurally similar to the δ-MnO_2 phase. Xie *et al.* found a very similar diffraction pattern for the MnO_x-coated MWNT and claimed it to be an ε-MnO_2 phase. This ε-MnO_2 phase can be described as a highly defective MnO_2 phase showing more de Wolff faults and microtwinning than γ-MnO_2 or rather a nearly random distribution of Mn ions in a hexagonally close packed O^{2-} lattice.[47]

In the case of i-MnO_x, the diffraction pattern exhibits more than 10 reflections arising from γ-MnO_2 (space group: *Pnma*; PDF#00-044-0142) and rutile-type β-MnO_2 (space group: $P4_2/mnm$, PDF#01-072-1984) as the major and minor phase, respectively. Crystallite size analysis from reflection broadening is generally hindered for β- and γ-MnO_2 because size-induced broadening is superimposed by defect-induced broadening of the reflections. Furthermore, the limited intensity of the reflections made crystallite size analysis for the γ-MnO_2 phase in i-MnO_x impossible. In the case of β-MnO_2, the (220) reflection at ~59° is not affected by defects in the rutile lattice and could be used to estimate the size of the β-MnO_2 crystallites to be below 5 nm.[30]

According to the diffraction pattern, the γ-MnO_2 phase of i-MnO_x exhibits a significant amount of single chains of Mn octahedra in the γ-MnO_2 lattice (de Wolff defects) and a minor fraction of twinning faults. The presence of de Wolff defects is visible in the significant shift of the (130) reflection at ~32° with more than 3° from its ideal position. De Wolff defects can reduce the angular separation of γ-MnO_2 (110) and (130) from 12 to 7°.[30] However, the γ-MnO_2 (110) reflection is hidden under the C reflection at ~25°. The presence of any sizeable contribution from an α-Mn_2O_3 phase in i-MnO_x (as a possible origin of the diffraction reflection at ~32°) was excluded from XAFS characterization discussed further below.

Microtwinning in the γ-MnO_2 lattice could be extracted from the merged (221)/(240) doublet of γ-MnO_2 at ~56° but the real fraction of microtwinning is significantly lower because higher microtwinning would lead to a shift of the (130) reflection towards higher diffraction angles, which was not observed in our data.

These findings from X-ray diffraction analysis are in agreement with earlier TEM analysis showing that s- and i-MnO_x consist of Mn oxide particles with a size <10 nm attached to the $MWNT_{ox}$.[24]

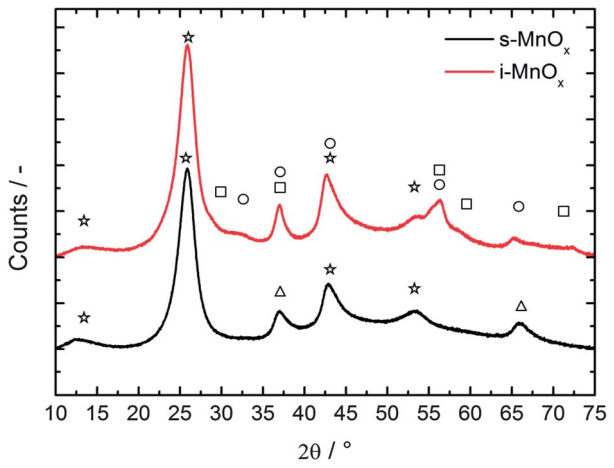

Fig. 2 Powder X-ray diffraction pattern of s-MnO_x (black) and i-MnO_x (red) between 10° and 75° using Cu K_α radiation. Reflections are labeled by squares for β-MnO_2, by circles for γ-MnO_2, by triangles for the layered MnO_2 phase, and by stars for the reflections caused by the support material. The latter are shown in Fig. S1.†

Manganese oxidation states from XANES spectra

To get further insights into the structure of the two catalytically active oxides at the atomic scale, we employed X-ray absorption spectroscopy at the Mn K-edge (Fig. 3).

The XANES (X-ray absorption near-edge structure) region is particularly sensitive to the average oxidation state and local coordination geometry.[48] In general, the energy of the X-ray absorption edge increases with increasing oxidation states of the absorbing atoms due to the rise in the electron binding energy.[49] On the basis of calibration with Mn compounds with known structures, the average oxidation state of manganese in i-MnO_x powder was around 3, while in s-MnO_x it was around 3.5. After deposition on the GC electrode the oxidation state in both s-MnO_x and i-MnO_x was estimated to be around 3.5 (Fig. S2 and S3†). This indicates that both oxides contain a large fraction of Mn^{4+} already before applying an oxidizing potential, but a significant amount of Mn ions are in a lower oxidation state (+2 or +3). The result for s-MnO_x is in good agreement with the

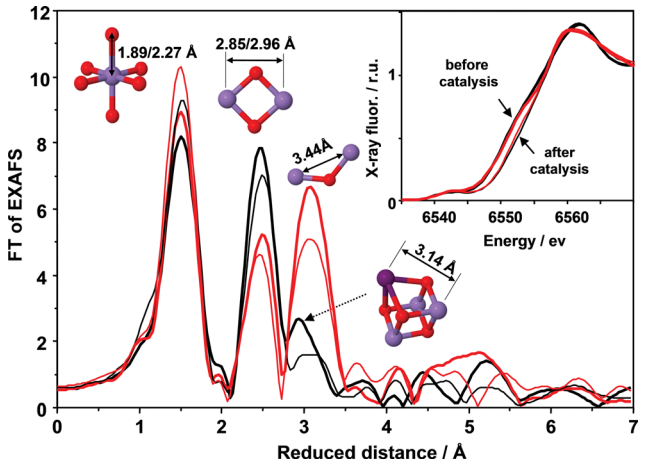

Fig. 3 X-ray absorption spectra of s-MnO_x (black) and i-MnO_x (red) deposited on electrodes before and after catalysis. The edge region of the spectra (XANES) is shown in the inset. The average oxidation state of Mn in the two samples directly after deposition on the electrode (thick lines) is around 3.5, while after 3 min of operation at 1.763 V in 0.1 M KPi at pH 7, it increases to 3.9–4.0 (thin lines). The structural motifs considered in the EXAFS simulations are schematically depicted next to the corresponding FT peak and the obtained interatomic distances are indicated. (Mn^{4+} ions are presented as spheres in magenta, Mn^{3+} ions in dark purple, and oxygen as red spheres.)

previously determined Mn oxidation state by Mn L-edge measurements and temperature-programmed reduction (TPR).[24] The oxidation state for i-MnO_x previously obtained from Mn L-edge XAS, however, was +2, explainable by Mn reduction occurring either during the thermal treatment at low oxygen partial pressure and or caused by X-ray irradiation during data collection. In the present study the thermal treatment was performed at 110 °C instead of 80 °C and in ambient air. X-ray photoreduction was avoided in the present study by (i) collecting the XAS spectra at a temperature of 20 K and (ii) using strictly limited periods of X-ray irradiation on a single sample spot.

For transition metal based catalysts, the oxidation state of the metal ion was suggested to depend on the applied potential during electrocatalytic OER.[15,21,50,51] To determine the extent of these changes for the Mn ions in the studied materials, we measured XAS spectra of s- and i-MnO_x frozen in liquid nitrogen immediately after applying 1.763 V in 0.1 M KPi at pH 7 for 3 min. In both oxides, a clear shift of the edge position in the XANES spectra was observed (Fig. S2†) corresponding to an increase of the mean Mn oxidation state to almost +4.0. The same shift in the edge position was observed for s-MnO_x frozen after 3 min of operation at 1.763 V in 0.1 M KOH at pH 13.

Despite the similar Mn oxidation state of the two oxides after operation as catalysts, the quasi-*in situ* experiment revealed differences in XAS edge shapes which imply that the coordination geometry of the Mn ions is modified. To address these structural differences, extended X-ray absorption fine-structure (EXAFS) spectra were analysed.

Structural information from EXAFS

The Fourier transforms (FTs) of the EXAFS spectra of s-MnO_x and i-MnO_x are presented in Fig. 3. In the FT, typically each peak corresponds to a specific absorber-backscatterer vector. In our case the absorber is a Mn ion, and the backscattering atoms can be either oxygen atoms or Mn ions surrounding the absorber. The distance between the absorber and backscatterer corresponds to the position of the FT peak plus about 0.4 Å.[48]

Both s-MnO_x and i-MnO_x show a first peak at a reduced distance of around 1.5 Å, which is typical for 6-fold oxygen coordinated Mn^{4+} ions and a second peak at around 2.5 Å related to di-μ-oxo-bridged Mn^{4+} ions.[52,53] For i-MnO_x there is also a well pronounced third peak, assignable to mono-μ-oxo-connected Mn ions (longer Mn–Mn distance).[54] This assignment of the first three peaks can be made by comparison to the FT spectra of Mn oxides with known structures (Fig. S4-B†). Visual comparison to the FTs of EXAFS spectra from reference Mn oxides suggests that while s-MnO_x has layered δ-MnO_2-like structure composed predominantly of edge-sharing (di-μ-oxo-connected) Mn octahedra (Fig. 5), the i-MnO_x contains a significant fraction of corner-sharing (mono-μ-oxo-connected) Mn octahedra resulting in formation of tunnels.

To confirm this interpretation and to analyse the structural changes during the electrochemical water oxidation, we simulated seven k^3-weighted EXAFS spectra measured from s-MnO_x and i-MnO_x (i) as powders, (ii) after deposition on the GC electrode, (iii) and after catalytic operation at 1.763 V *vs.* RHE at pH 7. The GC electrode covered with s-MnO_x was also measured after electrocatalytical operation at pH 13.

In the EXAFS simulations, we assumed two Mn–O distances contributing to the first Mn coordination shell: the shorter Mn–O distance is assigned to Mn^{4+}–O vectors and the longer is assignable either to Mn^{3+}–O vectors along the elongated Jahn–Teller axis or to Mn^{2+}–O vectors. The sum of the coordination

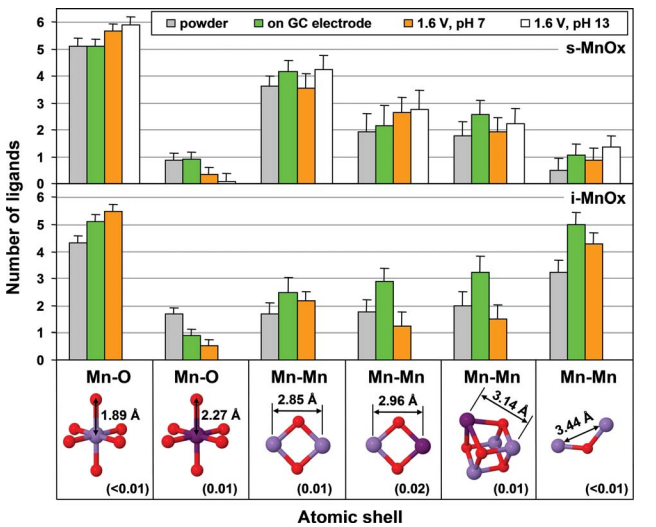

Fig. 4 Coordination numbers and interatomic distances obtained by joint simulation of the k^3-weighted EXAFS spectra from s-MnO_x (upper panel) and i-MnO_x (lower panel) before and after operation as water oxidation catalysts in 0.1 M KPi (pH 7) or 0.1 M KOH (pH 13). The corresponding absorber–backscatter distances were kept equal for all seven spectra and are displayed together with the corresponding structural motif (colour code as in Fig. 2). The error bars represent the 68% confidence interval; the error for the interatomic distances is given in parentheses below the corresponding structural motif. For further details, see Fig. S6.†

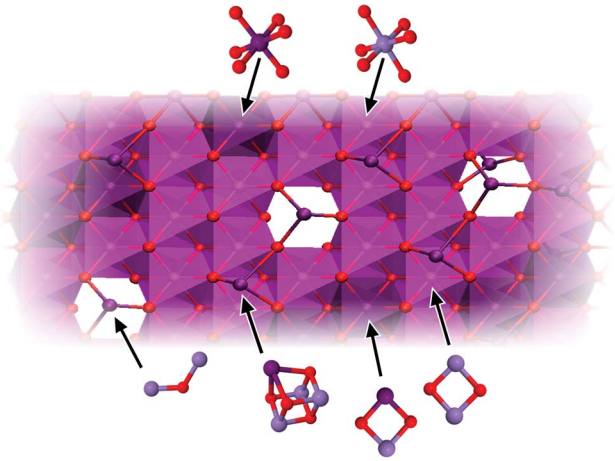

Fig. 5 Schematic model for a distorted MnO_x layer fragment formed from edge-sharing (di-μ-oxo-bridged) $Mn^{4+}O_6$ and $Mn^{3+}O_6$ octahedra. Some Mn ions from the layer are missing (defects), and other Mn ions are bound on top (or below) of the layer resulting in mono-μ-oxo-bridges (corner-sharing octahedra). At these defect sites, a row of edge-sharing octahedra could grow perpendicularly to the first one; this eventually may lead to formation of tunnel-like structures. Binding of Mn^{3+} ions on top of the layer at sites without layer defects results in formation of (distorted) Mn_4O_4 cubanes. (Mn^{4+} ions in magenta, Mn^{3+} ions in dark purple, and O in red.)

numbers for these two shells was kept equal to 6 because the small pre-edge feature of the XANES data suggested that in all samples the majority of the Mn ions are 6-fold coordinated. The other FT peaks were simulated with three shells of Mn backscatterer: a short Mn–Mn vector corresponding to edge-sharing MnO_6 octahedra (second peak), a longer Mn–Mn distance corresponding to corner-sharing MnO_6 octahedra (the third peak visible clearly in i-MnO_x samples) and an elongated di-μ-oxo-bridge, which could be hidden due to the large third peak in i-MnO_x but is visible in s-MnO_x. Such an intermediate distance was found in layered Mn oxides before and likely corresponds to Mn_4O_4 cubane motifs formed by the attachment of a Mn ion in an oxidation state lower than +4. Also in other water-oxidizing oxides, formation of a metal-oxo-cubane has been reported.[29,53] The simulation results shown in Fig. S5† confirm the qualitative interpretation given above and specify internuclear distances at high precision.

We approached identification of structural changes resulting from application of oxidising potential during operation of the electrocatalyst. In tendency, Mn–O distances were decreased after operation at 1.763 V, confirming the increase of the average Mn oxidation state implied by the XANES data. For the Mn–Mn vectors in the s-MnO_x sample, there appears no significant change in the coordination numbers, neither due to attachment to the GC electrode nor due to electrochemical treatment oxidation. For i-MnO_x, there is an increase in the EXAFS coordination of the Mn–Mn vectors caused by attachment to the electrode. Interestingly, application of an oxidizing potential decreases the number of Mn–Mn vectors. Although these changes appear to be significant, due to the large error bars an unambiguous statement about the extent and character of the structural changes cannot be made based on these fit results.

The EXAFS fit results in a *mean* Mn–Mn distance of (2.89 ± 0.01) Å between the Mn nuclei of two edge-sharing MnO_6 octahedra. The XANES data show the prevalence of Mn^{4+} but also Mn^{3+} ions may be present. For di-μ-oxo-bridged Mn^{4+} ions, the obtained Mn–Mn is often shorter, namely 2.86 Å.[21,53,55,56] Moreover, we find that the Debye–Waller (DW) parameter corresponding to this shell is unusually high (Fig. S5-C†) indicating either a broad Gaussian-shaped distance distribution function or a bimodal distribution, both centred around a mean Mn–Mn distance of 2.89 Å. The latter option is clearly more likely and implies that there are two specific Mn–Mn distances which contribute to the second FT peak. The shorter (<2.89 Å) and the longer one (>2.89 Å) may be assignable to Mn^{4+}–$(\mu\text{-O})_2$–Mn^{4+} and Mn^{4+}–$(\mu\text{-O})_2$–Mn^{3+} motifs, respectively.[29,56] For more refined analysis, we approached a 'joint-fit' of all seven EXAFS spectra keeping the interatomic distances for the corresponding shells equal in all spectra. The increased significance of the joint-fit approach facilitated, *inter alia*, resolution of two short Mn–Mn distances of 2.85 and 2.96 Å, respectively. The joint-fit results are shown in Fig. 4 and discussed in the following.

In the first Mn coordination sphere, short 1.89 Å Mn–O vectors typical for 6-fold coordinated Mn^{4+} are prevalent. A small fraction of up to 15% longer Mn–O distances of 2.29 Å is consistent with a minor contribution of Mn^{2+} or Mn^{3+} ions (for Mn^{3+} ions such long Mn–O distances are found along the Jahn–Teller axis).[57,58]

The results of the joint-fit approach (Fig. 4) confirm the absence of major structural change for s-MnO_x. After catalyst operation at 1.763 V, there may be a slight decrease in the number of the out-of-layer Mn^{3+} ions (cubane motifs, 3.14 Å) and a slight increase of the in-layer Mn^{3+} ions (2.96 Å), resulting in larger heterogeneity of the Mn–Mn distances contributing to the second FT peak and thus a decreased peak height. These changes are relatively small and thus close to the error limit. The sum of the two short Mn–Mn vectors is around 6 as expected for perfectly ordered layers of δ-MnO_2.[53] Interestingly, this value appears to increase slightly upon catalyst operation at 1.763 V, possibly explainable by Mn–Mn vectors from out-of-layer Mn^{4+} ions involved in $Mn^{4+}{}_4(\mu O)_4$ cubane formation.

When an oxidizing potential is applied to i-MnO_x, larger structural rearrangements can be observed (Fig. 4). There is a clear decrease of the mono-μ-oxo and di-μ-oxo-vectors with participation of Mn^{3+} ions (2.96 Å and 3.14 Å distances). This decrease in the number of in-layer Mn^{3+} ions (2.96 Å) contrasts the slight increase in s-MnO_x. Also the Debye–Waller parameter (distance spread) for the Mn–O distances increases at higher potential for s-MnO_x and decreases for i-MnO_x (Fig. S6†), which could reflect different protonation patterns of the oxygen atoms at bridging and terminal positions.

The presented results indicate clear differences between the structure of the two oxides in their resting states (XRD, EXAFS) and regarding the structural changes induced by application of an oxidizing potential (EXAFS). The question arises of whether and how these structural differences relate to the elementary mechanism of the water oxidation and oxygen evolution. To investigate this further, s-MnO_x and i-MnO_x were characterized

electrochemically and indeed, confirmation for different processes involved in water oxidation was found in the different kinetic characteristics of the two materials, as described in the following.

Electrochemical and electrokinetic characterization

Electrochemical characterization. Cyclic voltammetry was used to investigate the redox behaviour of the Mn ions in s- and i-MnO_x in 0.1 M KPi at pH 7. Fig. 6 shows the first and the 11th potential scan recorded between 1.0 and 1.7 V at a scan rate of 100 mV s^{-1} with a starting potential of 1.5 V. Both materials exhibited a mainly capacitive voltammogram between 1.0 and 1.6 V caused by the charge storage capability of both the high-surface carbon support and MnO_x. The capacitance of s-MnO_x is clearly larger than that of i-MnO_x, which does exceed the capacitance of the carbon support only marginally (Fig. S8†). This suggests a higher extent of oxidative charging (by Mn oxidation) in s-MnO_x. At potentials above 1.6 V, the current increases *inter alia* due to oxygen evolution.

Both voltammograms show the differences in the redox behaviour of the Mn ions in MnO_x. The first cathodic potential scan of both MnO_x exhibits a double reduction feature (MnR-1 and MnR-2) between ~1.45 and 1.10 V. During the subsequent anodic scan, s-MnO_x exhibits the corresponding oxidation peak whereas no oxidation peak is resolved for i-MnO_x. The transferred charge during electrochemical reduction of the Mn ions in i-MnO_x is significantly lower. Comparing the potential of the reduction feature of s- and i-MnO_x with literature values might point toward the redox couple of Mn^{2+}/MnO_2.[59] This assignment is in line with the XANES results which show that at an OER potential mainly Mn^{4+} ions are present in the catalyst. However, the presence of a double reduction feature in s- and i-MnO_x suggests a two-step electrochemical reduction of Mn^{4+} to Mn^{3+} and further on to Mn^{2+}. In electrodeposited MnO_x films, similar redox peaks were successfully connected to changes in the visible light absorption of the oxide and interpreted as Mn oxidation state changes.[21]

During continuous potential cycling between 1.0 and 1.7 V, the Mn^{4+} reduction features disappear completely in the case of i-MnO_x whereas s-MnO_x continues to exhibit both redox features even after 10 potential cycles with only slightly reduced charge. Thus, the Mn ions in i-MnO_x passivate irreversibly (but notably not completely) during initial reduction and the voltammogram becomes almost purely capacitive, whereas we observe only little redox passivation in s-MnO_x.

Tafel slope analysis. Fig. 7 shows Tafel plots for s- and i-MnO_x extracted from quasi-stationary experiments in 0.1 M phosphate buffer at pH 7. (In Fig. 7 and elsewhere, the detected electrical current is given; the current density per cm^2 is by a factor of about 5 higher than the indicated current.) Both s- and i-MnO_x show a linear E *vs.* log(I) dependency in the potential range of 1.6–1.9 V and 1.7–1.9 V, respectively. The onset potential for the electrocatalytic oxygen evolution is ~100 mV lower for s- than that of i-MnO_x. A linear regression of the experimental data within the mentioned potential ranges led to Tafel slopes of 158 and 109 mV dec^{-1} and thus, experimental anodic transfer coefficients, β, of 0.39 and 0.54 for s- and i-MnO_x, respectively. The exchange current density i_0 of s-MnO_x (~10^{-3} mA) is significantly higher than that of i-MnO_x (~10^{-7} mA). Thus, s-MnO_x shows a significantly higher intrinsic electrocatalytic activity than that of i-MnO_x, whereas at higher electrode potentials the OER activity of i-MnO_x is superior. Thus, we conclude conservatively that there are pronounced functional differences between s-MnO_x and i-MnO_x in the rate-determining process and possibly regarding number and location of active sites.

pH dependence of overpotential and current. Fig. 8 shows the dependence of the overpotential, η, on the H^+/OH^- concentration in the electrolyte between pH 5 and ~12 at a constant current of 20 μA and 50 μA. At both currents, the η–pH profile for both MnO_x can be divided into two regimes. For example at a constant current of 20 μA (Fig. 8b), the overpotential increases between pH 5 and 9.6 for s-MnO_x (i-MnO_x) from 435 mV (495 mV) to 497 mV (574 mV). Above pH 10, the overpotential decreases to 441 mV (495 mV). Thus at 20 μA, s-MnO_x exhibits a lower overpotential over the investigated pH

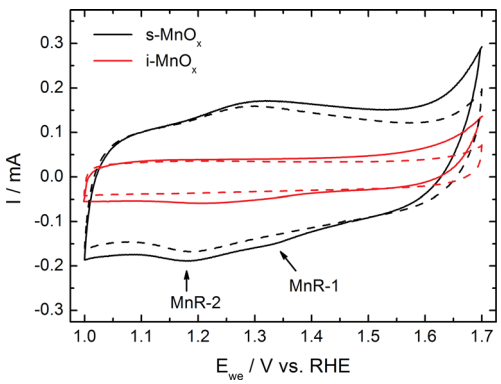

Fig. 6 Cyclic voltammograms (CV) of the first (solid) and 11th (dashed) scan of s-MnO_x (black) and i-MnO_x (red). The CVs were recorded in 0.1 M KPi at pH 7 with a scan rate of 100 mV s^{-1}. Two minima resolved in the s-MnO_x CV are labelled by MnR-1 and MnR-2, respectively.

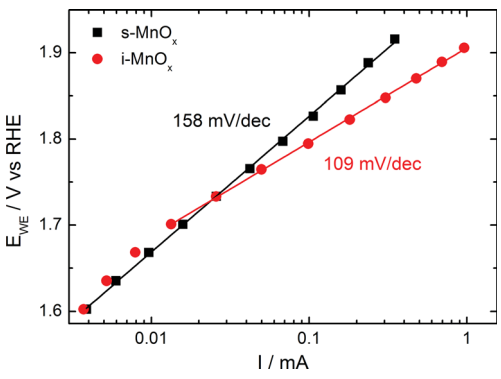

Fig. 7 Tafel plot of s-MnO_x (black) and i-MnO_x (red) extracted from quasi-stationary potential-step RDE experiments in 0.1 M KPi at pH 7. All electrode potentials have been iR-corrected. The respective Tafel slopes as determined by linear regression are indicated.

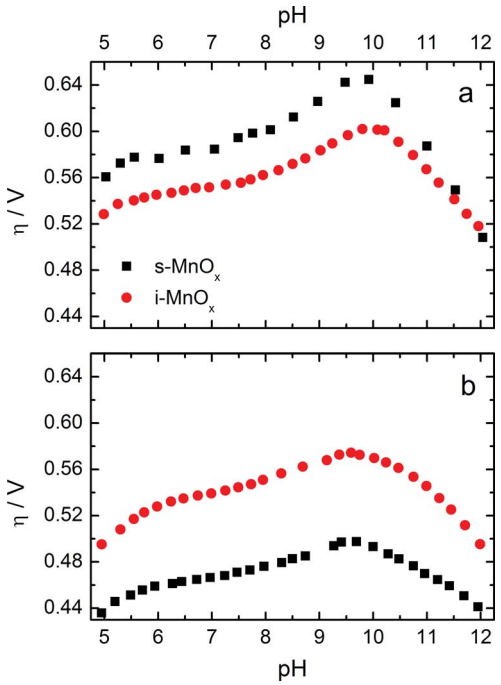

Fig. 8 pH dependency of the overpotential (η) of s- and i-MnO_x determined in 0.1 M KPi at constant currents of (a) 50 μA and (b) 20 μA. The overpotential has been calculated according to eqn (S1).†

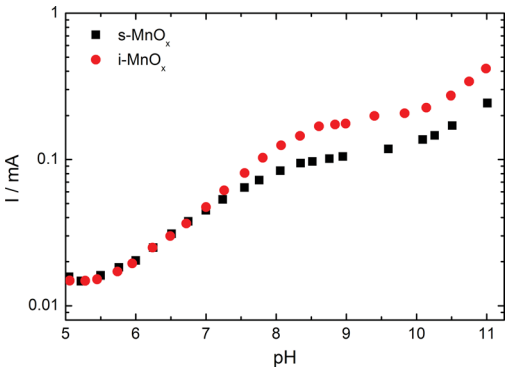

Fig. 9 pH dependence of the catalytic current (I) determined in 0.1 M KPi at a constant electrode potential of 1.35 V *vs.* NHE.

range than i-MnO_x, due to its higher intrinsic electrocatalytic activity (higher exchange current density), but the principal pH dependence of the catalytic current of two oxides is the same. At 50 μA (Fig. 8a), i-MnO_x exhibits a lower overpotential, due to its lower Tafel slope. Yet again, the principal pH dependence of the two oxides is the same. Thus, we conclude that an intricate coupling of electrocatalysis to (de)protonation reactions is functionally decisive in both oxides. Comparison of the two panels of Fig. 8 reveals that the crossover point of the Tafel plot is observable at all investigated pH values implying that at all pH, the exchange current in s-MnO_x is higher than that in i-MnO_x whereas the Tafel slope always is lower in i-MnO_x. This implies that the functional differences between the two oxides indicated by different Tafel slopes and exchange currents do *not* relate to differences in the coupling of the rate-determining step to protonation reactions.

We also investigated the pH-dependence of the current at a constant catalytic potential of 1.35 V *vs.* NHE (Fig. 9). With increasing pH, a biphasic increase in the catalytic current is observed. The first increase is detected for pH values ranging from 5.7 to 8.7, that is, around the second pK of the phosphate ion ($pK_{2nd} = 7.2$, $H_2PO_4^{1-} \leftrightarrow HPO_4^{2-} + H^+$); at pH values below 5.7 and above 8.2, plateau levels are reached. Thus the pH dependence of the catalytic current at a constant potential of 1.35 V *vs.* NHE resembles the pH titration curve of the phosphate ion. This finding suggests that stoichiometry or concentrations of $[HPO_4^{2-}]$ and $[H_2PO_4^{1-}]$ determine catalytic activity. At even higher pH (>10), a further increase is observed, explainable by the increasing availability of OH^- ions at higher pH values.

Discussion

The oxygen evolution reaction is a complex multi-electron transfer process controlled by macroscopic, microscopic and atomistic parameters, such as the number, accessibility and character of catalytically active sites, the chemical reaction mechanism, the concentration of reactant, electrical and protonic conductivities and the removal of products.

The number of catalytically active sites depends on the number of accessible Mn ions for water molecules, which, in turn, is strongly connected to the structure and the morphology of the electrocatalyst. If no Mn ions of the bulk material were involved in the water splitting, the number of active sites would be (most probably) directly proportional to the surface area of MnO_x and thus, particle size. However, in the case of a layered MnO_2 phase, bulk Mn ions are accessible for water molecules and cations alike and thus, the number of accessible active sites is more likely approaching the total number of Mn ions. Furthermore, the local coordination of the Mn ions can critically determine how accessible they are and to what extent they can contribute to the overall catalytic activity.

For the two nano-structured Mn oxide catalysts considered herein, there is a clear and important structural difference in the Mn coordination, *e.g.* there exist nearly exclusively di-μ-oxo-bridged Mn ions in s-MnO_x, whereas more mono- than di-μ-oxo-bridged Mn ions exist in the i-MnO_x catalyst. The electrochemical analysis suggests that higher intrinsic onset activity in the low-current regime is associated with the prevalent presence of di-μ-oxo-bridged Mn ions in form of a layered oxide (Fig. 1c) coupled with a significantly higher electrochemical capacitance. Thus, we hypothesize that the electrochemical accessibility of catalytically active Mn ions, likely one important controlling factor for OER activity, is higher in the layered s-MnO_x structures than in the cross-linked i-MnO_x structures. This is consistent with the fact that in layered δ-like MnO_2 structures bulk Mn ions are much better accessible for the reactant molecules and cations through the interlayer space. This is in clear contrast to tunnelled MnO_2 structures which generally show a lower charge storage capacity compared to layered Mn structures and the charge storage capacity is proportional to the void space in the lattice. The (1 × 1) and (2 × 1) tunnels in i-MnO_x exhibit certain proton conductivity but are not

accessible to the water molecules and larger cations.[35,60] In conclusion, the participation of bulk Mn ions could lead to a larger number of active sites and thus, a higher exchange current density for s-MnO_x than i-MnO_x.

The structural motif of di-μ-oxo-bridged transition metal ions resulting in layers (or layer fragments) of edge-sharing MO_6 octahedra has proven to be a unifying feature of many oxygen-evolving Co and Ni oxide electrocatalysts prepared by electrodeposition.[12,14,15,17] Looking at electrodeposited OER catalyst materials, the beneficial effect of layered oxide with the prevalence of di-μ-oxo-bridging between metal ions and their large interlayer space filled by water and further ions becomes obvious: bulk metal ions are able to participate as catalytically active sites.[15]

Beyond its favourable intrinsic activity (high exchange current density), Tafel slope analysis showed that layered s-MnO_x displayed inferior electrocatalytic behaviour at larger current densities reflected by a larger Tafel slope of 158 mV dec^{-1} compared to 109 mV dec^{-1} for i-MnO_x. The unfavourably large Tafel slope of s-MnO_x likely relates to the high level of order within the layers of edge-sharing MnO_6 octahedra, which is clearly higher than those found in the electrodeposited MnO_x of ref. 21 (a Tafel slope of 90 mV dec^{-1}) and in water-oxidizing MnO_x particles.[21,29] Less order implies a higher number of defect sites, *e.g.* Mn vacancies; the structures of putative defect sites are shown in Fig. 5. These defect sites prevent the prevalence of di-μ_3-oxo thereby resulting in more di-μ_2-O(H) bridges between Mn ions as well as in a higher number of terminal water coordination sites; both features likely are crucial for OER activity.[3] And indeed, an inverse relationship between di-μ_3-O bridging (low number of di-μ_2-O(H) bridges and defect sites in general) and OER activity has been demonstrated for Co- and Mn-based oxides before,[15,21,22] but a comparison of Tafel slopes had not been approached. We now propose that an unfavourably high Tafel slope of the OER reaction can result from a strong prevalence of unreactive di-μ_3-oxo-bridges between the first-row transition metal ions of the respective oxide, which is caused by the octahedral cross-linking and/or a level of structural order that is too high. This suggestion is supported by the results of the present investigation and immediately provides a guideline for designing catalytic oxides with a favourably low Tafel slope. We note in passing that di-μ_2-oxo-bridges are also present at the ideal β-MnO_2(110) and γ-MnO_2(100) surfaces and so, similar structural motifs could participate in the electrocatalysis of s-MnO_x ('internal' surface between oxide fragment and intercalated water) as well as of i-MnO_x ('external' oxide-electrolyte surface).

Tafel slopes of ~120 mV dec^{-1} have been determined for Mn oxide electrocatalysts and from this, a one-electron transfer step has been concluded to be the rate-determining step (rds) in MnO_x.[26] Herein, a lower Tafel slope of 109 mV dec^{-1} as determined for i-MnO_x does not support a simple one-electron transfer step to be rate determining during OER, neither does the value of 158 mV dec^{-1} in s-MnO_x. In line with this conclusion, the detected pH-dependence of overpotential and catalytic current rule out rate-limitation by a simple one-electron transfer step, but point towards a role of proton-coupled electron transfer in the rds.

A critical factor determining the OER activity is ion transport, specifically proton removal from the catalytic site and proton transfer into the electrolyte. Relevant factors may be the proton conductivity and uptake capability of the electrolyte. The log(I)–pH profile of Fig. 9 reflects the 2nd phosphate pK, thereby illustrating a crucial role of the phosphate protonation state. In the η–pH profile of Fig. 8, we find a minimal catalytic activity at a maximal concentration of HPO_4^{2-} equivalent to the minimal buffer strength in the investigated pH range (Fig. S12†). The buffer strength is the ability to compensate for increasing H^+ concentration by chemical binding of the proton to a base. At pH values above the 2nd phosphate pK (pK_{2nd} ≈ 7.2), the buffer strength of the $HPO_4^{2-}/H_2PO_4^{1-}$ ion decreases. At higher pH, the hydroxyl ions can significantly contribute to the proton uptake and the buffer strength increases. Both effects are reflected in the η–pH curves of both oxides. The beneficial influence of the phosphate buffer is not related to an increase of the proton conductivity of the bulk solution. Though there are changes in the conductivity of the electrolyte (Fig. S11a†), the iR-correction does not change the η–pH profile significantly (Fig. S11b†). The chemical proton abstraction from the active site by phosphate ions either adsorbed to MnO_x or in solution within the Helmholtz layer appears to be decisive. Thus, Mn-based catalyst materials containing sizeable amounts of a proton-accepting base either as an intrinsic constituent – as reported for the 'cobalt-phosphate catalyst'[9] – or formed during operation may be a promising strategy.

Conclusions

We have revealed the dominant atomic-scale structural motifs of two distinctly different, either layered or 3D cross-linked, water-oxidizing MnO_x catalysts, and succeeded in correlating these structure motifs with the respective catalytic activity. Such relationships are of general importance, since they enable us to identify critical oxide characteristics controlling electrocatalytic activity.

Our investigation suggests that the deliberate formation of activity controlling structural motifs can be controlled by simple conventional liquid metal ion precursor chemistry and is not restricted to electrodeposition methods.

The electrokinetic analysis showed that the apparent processes during water oxidation depend on the different octahedral cross-linking in MnO_x (with essentially the same mean oxidation state of the Mn ions), as clearly reflected in the two pronouncedly different Tafel slopes. The comparison to the structural data suggests that the atomic structure is a crucial determinant of the apparent processes during OER catalysis. Comparison with electrodeposited electrocatalysts guides towards a general character of MnO_x OER electrocatalysts.

The active catalyst states of both MnO_x are closely related to the catalyst "precursor" although the mean Mn oxidation state increases from 3.5 to ~4 upon operation at catalytic potential. Specifically, clear indications for Mn–Mn bridging mode changes in i-MnO_x upon oxidation of the catalyst are detectable. This important discovery requires further in-depth investigation before its discussion in terms of the mechanism of water

oxidation in the Mn oxides can be approached. We also note the interesting structural analogy between out-of-layer Mn ions linked to in-layer Mn ions *via* mono-μ-oxo-bridges resulting in corner-sharing MnO_x octahedra and coordinatively unsaturated sites (cus) metal ion sites in rutile surfaces. It is feasible that coordinative undersaturation of such out-of-layer Mn ions may confer favorable adsorption and catalytic reaction characteristics as found for rutile cus sites.[61,62]

Furthermore, our studies unravelled the beneficial effect of the proton uptake capability of the phosphate buffer during water splitting due to buffer strength and OH^- concentration. These findings – and the complex pH dependence in general – illustrate the importance of proton abstraction in OER catalysis by the two herein investigated oxides. However, further studies especially on the interaction between phosphate and MnO_x with respect to OER are necessary.

In summary, the structure–activity insights from this study provide guidelines to design and control the electrochemical OER behaviour of the complex structural chemistry of non-precious transition metal oxides. The water accessibility of the bulk oxide and the number of defect sites were tentatively identified as determinants of the experimental exchange current density and Tafel slope, respectively. The presented work may pave the way for future investigations which eventually could result in a comprehensive understanding of structure–activity relationships in water-oxidizing Mn oxides at the atomistic level.

Acknowledgements

We thank K. Mette (FHI) for collaboration regarding the synthesis, Dr P. Chernev, Dr M. Risch and J. Heidkamp (Freie Universität Berlin) for contributing to data collection at the synchrotron radiation source as well as M. Mertin and Dr F. Schäfers for their excellent technical support at the beamline KMC-1 of the BESSY, a synchrotron radiation source in Berlin operated by the Helmholtz-Zentrum Berlin. Financial support by the Berlin cluster of excellence on Unifying Concepts in Catalysis (UniCat) is gratefully acknowledged. Arno Bergmann acknowledges financial support by the Berlin Graduate school of Natural Sciences and Engineering (BIG-NSE).

References

1 J. O. M. Bockris, *Int. J. Hydrogen Energy*, 1999, **27**, 731–740.
2 T. A. Faunce, S. Styring, M. Wasielewski, G. Brudvig, B. Rutherford, J. Messinger, A. F. Lee, C. L. Hill, H. de Groot, M. Fontecave, D. MacFarlane, B. Hankamer, D. G. Nocera, D. M. Tiede, H. Dau, W. Hillier and L. Wang, *Energy Environ. Sci.*, 2013, **6**, 1074–1076.
3 H. Dau, C. Limberg, T. Reier, M. Risch, S. Roggan and P. Strasser, *ChemCatChem*, 2010, **2**, 724–761.
4 T. Reier, M. Oezaslan and P. Strasser, *ACS Catal.*, 2012, **2**, 1765–1772.
5 R. Forgie, G. Bugosh, K. C. Neyerlin, Z. Liu and P. Strasser, *Electrochem. Solid-State Lett.*, 2010, **13**, B36–B39.
6 K. C. Neyerlin, G. Bugosh, R. Forgie, Z. Liu and P. Strasser, *J. Electrochem. Soc.*, 2009, **156**, B363–B369.
7 N. Menzel, E. Ortel, R. Kraehnert and P. Strasser, *ChemPhysChem*, 2012, **13**, 1385–1394.
8 E. Ortel, T. Reier, P. Strasser and R. Kraehnert, *Chem. Mater.*, 2011, **23**, 3201–3209.
9 M. W. Kanan and D. G. Nocera, *Science*, 2008, **321**, 1072–1075.
10 A. J. Esswein, Y. Surendranath, S. Y. Reece and D. G. Nocera, *Energy Environ. Sci.*, 2010, **4**, 499–504.
11 J. B. Gerken, J. G. McAlpin, J. Y. C. Chen, M. L. Rigsby, W. H. Casey, R. D. Britt and S. S. Stahl, *J. Am. Chem. Soc.*, 2011, **133**, 14431–14442.
12 M. Risch, V. Khare, I. Zaharieva, L. Gerencser, P. Chernev and H. Dau, *J. Am. Chem. Soc.*, 2009, **131**, 6936–6937.
13 Y. Surendranath, M. W. Kanan and D. G. Nocera, *J. Am. Chem. Soc.*, 2010, **132**, 16501–16509.
14 M. W. Kanan, J. Yano, Y. Surendranath, M. Dincâ, V. K. Yachandra and D. G. Nocera, *J. Am. Chem. Soc.*, 2010, **132**, 13692–13701.
15 M. Risch, K. Klingan, F. Ringleb, P. Chernev, I. Zaharieva, A. Fischer and H. Dau, *ChemSusChem*, 2012, **5**, 542–549.
16 M. Dincâ, Y. Surendranath and D. G. Nocera, *Proc. Natl. Acad. Sci. U. S. A.*, 2010, **107**, 10337–10341.
17 M. Risch, K. Klingan, J. Heidkamp, D. Ehrenberg, P. Chernev, I. Zaharieva and H. Dau, *Chem. Commun.*, 2011, **47**, 11912–11914.
18 J. O. Bockris and T. Otagawa, *J. Phys. Chem.*, 1983, **87**, 2960–2971.
19 P. C. K. Vesborg and T. F. Jaramillo, *RSC Adv.*, 2012, **2**, 7933–7947.
20 Y. Gorlin and T. F. Jaramillo, *J. Am. Chem. Soc.*, 2010, **132**, 13612–13614.
21 I. Zaharieva, P. Chernev, M. Risch, K. Klingan, M. Kohlhoff, A. Fischer and H. Dau, *Energy Environ. Sci.*, 2012, **5**, 7081–7089.
22 I. Zaharieva, M. M. Najafpour, M. Wiechen, M. Haumann, P. Kurz and H. Dau, *Energy Environ. Sci.*, 2011, **4**, 2400–2408.
23 V. B. R. Boppana and F. Jiao, *Chem. Commun.*, 2011, **47**, 8973–8975.
24 K. Mette, A. Bergmann, J.-P. Tessonnier, M. Hävecker, L. Yao, T. Ressler, R. Schlögl, P. Strasser and M. Behrens, *ChemCatChem*, 2012, **4**, 851–862.
25 F. Jiao and H. Frei, *Chem. Commun.*, 2010, **46**, 2920–2922.
26 M. Morita, C. Iwakura and H. Tamura, *Electrochim. Acta*, 1977, **22**, 325–328.
27 M. Morita, C. Iwakura and H. Tamura, *Electrochim. Acta*, 1979, **24**, 639–643.
28 M. Morita, C. Iwakura and H. Tamura, *Electrochim. Acta*, 1979, **24**, 357–362.
29 M. Wiechen, I. Zaharieva, H. Dau and P. Kurz, *Chem. Sci.*, 2012, **3**, 2330–2339.
30 Y. Chabre and J. Pannetier, *Prog. Solid State Chem.*, 1995, **23**, 1–130.
31 J. H. Albering, in *Handbook of Battery Materials*, ed. J. O. Besenhard, Wiley-VCH Verlag GmbH, 1999, pp. 85–112.
32 J. E. Post, *Proc. Natl. Acad. Sci. U. S. A.*, 1999, **96**, 3447–3454.
33 P. de Wolff, *Acta Crystallogr.*, 1959, **12**, 341–345.
34 S. Turner and P. R. Buseck, *Nature*, 1983, **304**, 143–146.

35 P. Rüetschi, *J. Electrochem. Soc.*, 1984, **131**, 2737–2744.
36 P. Rüetschi, *J. Electrochem. Soc.*, 1988, **135**, 2657–2663.
37 P. Rüetschi and R. Giovanoli, *J. Electrochem. Soc.*, 1988, **135**, 2663–2669.
38 Y. Mo, Y. Hu, I. T. Bae, B. Miller, M. R. Antonio and D. A. Scherson, *J. Electrochem. Soc.*, 1997, **144**, 1598.
39 H. Dau, I. Zaharieva and M. Haumann, *Curr. Opin. Chem. Biol.*, 2012, **16**, 3–10.
40 M. M. Najafpour, T. Ehrenberg, M. Wiechen and P. Kurz, *Angew. Chem.*, 2010, **122**, 2281–2285.
41 R. K. Hocking, R. Brimblecombe, L.-Y. Chang, A. Singh, M. H. Cheah, C. Glover, W. H. Casey and L. Spiccia, *Nat. Chem.*, 2011, **3**, 461–466.
42 R. Brimblecombe, A. Koo, G. C. Dismukes, G. F. Swiegers and L. Spiccia, *J. Am. Chem. Soc.*, 2010, **132**, 2892–2894.
43 T. Takashima, K. Hashimoto and R. Nakamura, *J. Am. Chem. Soc.*, 2012, **134**, 1519–1527.
44 R. Alessio, D. B. Dell'Amico, F. Calderazzo, U. Englert, A. Guarini, L. Labella and P. Strasser, *Helv. Chim. Acta*, 1998, **81**, 219–230.
45 M. Eiswirth, J. Bürger, P. Strasser and G. Ertl, *J. Phys. Chem.*, 1996, **100**, 19118.
46 Z. Liu, C. Yu, I. Rusakova, D. Huang and P. Strasser, *Top. Catal.*, 2008, **49**, 241–250.
47 X. Xie and L. Gao, *Carbon*, 2007, **45**, 2365–2373.
48 J. E. Penner-Hahn, *Coord. Chem. Rev.*, 1999, **190–192**, 1101–1123.
49 H. Dau, P. Liebisch and M. Haumann, *Anal. Bioanal. Chem.*, 2003, **376**, 562–583.
50 J. G. McAlpin, Y. Surendranath, M. Dincă, T. A. Stich, S. A. Stoian, W. H. Casey, D. G. Nocera and R. D. Britt, *J. Am. Chem. Soc.*, 2010, **132**, 6882–6883.
51 D. K. Bediako, B. Lassalle-Kaiser, Y. Surendranath, J. Yano, V. K. Yachandra and D. G. Nocera, *J. Am. Chem. Soc.*, 2012, **134**, 6801–6809.
52 A.-C. Gaillot, D. Flot, V. A. Drits, A. Manceau, M. Burghammer and B. Lanson, *Chem. Mater.*, 2003, **15**, 4666–4678.
53 T. G. Spiro, J. R. Bargar, G. Sposito and B. M. Tebo, *Acc. Chem. Res.*, 2010, **43**, 2–9.
54 S. M. Webb, B. M. Tebo and J. R. Bargar, *Am. Mineral.*, 2005, **90**, 1342–1357.
55 I. Saratovsky, P. G. Wightman, P. A. Pasten, J.-F. Gaillard and K. R. Poeppelmeier, *J. Am. Chem. Soc.*, 2006, **128**, 11188–11198.
56 S. M. Webb, B. M. Tebo and J. R. Bargar, *Am. Mineral.*, 2005, **90**, 1342–1357.
57 S. Geller, *Acta Crystallogr., Sect. B: Struct. Crystallogr. Cryst. Chem.*, 1971, **27**, 821–828.
58 R. E. Pacalo and E. K. Graham, *Phys. Chem. Miner.*, 1991, **18**, 69–80.
59 *Handbook of Chemistry and Physics*, ed. D. R. Lide, CRC-Press, 2001.
60 O. Ghodbane, J.-L. Pascal and F. Favier, *ACS Appl. Mater. Interfaces*, 2009, **1**, 1130–1139.
61 H. Over, *Chem. Rev.*, 2012, **112**, 3356–3426.
62 H. Over, *Electrochim. Acta*, 2013, **93**, 314–333.